Application of in-situ nano-scanning calorimetry and X-ray diffraction to characterize Ni–Ti–Hf high-temperature shape memory alloys

Citation	McCluskey, Patrick J., Kechao Xiao, John M. Gregoire, Darren Dale, and Joost J. Vlassak. 2015. "Application of in-Situ Nano-Scanning Calorimetry and X-Ray Diffraction to Characterize Ni–Ti–Hf High-Temperature Shape Memory Alloys." Thermochimica Acta 603 (March): 53–62. doi:10.1016/j.tca.2014.07.023.
Published Version	doi:10.1016/j.tca.2014.07.023
Citable link	http://nrs.harvard.edu/urn-3:HUL.InstRepos:22068309
Terms of Use	This article was downloaded from Harvard University's DASH repository, and is made available under the terms and conditions applicable to Open Access Policy Articles, as set forth at http://nrs.harvard.edu/urn-3:HUL.InstRepos:dash.current.terms-of-use#OAP

Application of in-situ nano-scanning calorimetry and x-ray diffraction to characterize Ni-Ti-Hf high-temperature shape memory alloys

Patrick J. McCluskey[1, a, b], Kechao Xiao[2], John M. Gregoire[3, b], Darren Dale[4], Joost J. Vlassak[2]

[1]*GE Global Research, One Research Circle, Niskayuna, NY 12309, USA*

[2]*School of Engineering and Applied Sciences, Harvard University, 29 Oxford Street, Cambridge, MA 02138, USA*

[3]*Joint Center for Artificial Photosynthesis, California Institute of Technology, 1200 E. California Blvd., Pasadena, CA 91125, USA*

[4]*Cornell High Energy Synchrotron Source, Ithaca, NY 14853, USA*

Abstract: Combinatorial nanocalorimetry and synchrotron x-ray diffraction were combined to study the martensite-austenite (M-A) phase transformation behavior of Ni-Ti-Hf shape memory alloys. A thin-film library of Ni-Ti-Hf samples with a range of compositions was deposited on a parallel nano-scanning calorimeter device using sputter deposition. Crystallization of each amorphous as-deposited sample by local heating at approximately 10^4 K/s produced a nanoscale grain structure of austenite and martensite. Individual samples were then cycled through the M-A transformation, while the transformation enthalpy was measured by nanocalorimetry and the low- and high-temperature phase compositions were determined by x-ray diffraction. The techniques enable correlation of the observed behavior during thermal cycling with the thermodynamic and structural properties of the samples.

Introduction

Continued development of integrated circuits, storage devices, sensors, and micro-electro-mechanical system increases the need to understand thermal properties of materials at reduced length scales. In many of these devices, precise knowledge of the thermo-physical properties of the materials is critical for proper operation. A few examples include phase-change memory materials, thermo-mechanical actuators, and thermal sensors. As feature sizes decrease, surface and interface energies become increasingly important, leading to thermo-physical behavior that is not well described by bulk

properties. Basic materials research must be performed at the relevant length scale, requiring the development of new instruments that outperform standard bulk materials characterization techniques.

Nanocalorimeter sensors significantly improve the capability of studying nanoscale materials by reducing the calorimeter addendum and therefore increasing sensitivity [Efremov 2004, Olson 2003, Minakov 2005, Queen 2009]. Such devices have a heat capacity on the order of 100 nJ/K and a thermal conductance on the order of 1 nWm/K, resulting in sensitivities on the order of 10 nJ/K. Differential measurement schemes can increase the sensitivity even further. Early studies using nanocalorimeters include the melting point depression of metallic nanoparticles [Efremov 2000, Zhang 2000, Lai 1996], structural changes in poly(ethylene terephthalate) [Minakov 2004], and heat capacity measurements in high magnetic fields (8 T) [Zink 2002]. The small heat capacity of these sensors also means that high heating rates are readily achieved, on the order of 10^5 K/s, which reduces measurement times by up to 5 orders of magnitude compared to traditional calorimetry.

Short measurement times and micromachining fabrication techniques make nano-scanning calorimetry (nSC) ideally suited for high-throughput measurements on thin-film samples [McCluskey 2006]. Micromachining techniques allow fabrication of nanocalorimeter-sensors arrays that can be used to analyze libraries of samples with unique compositions, synthesized using thin-film deposition techniques [McCluskey 2010a, Yahya 2011, Gregoire 2012]. High-throughput measurements necessarily involve many more measurements than the typical one-at-a-time approach and measurements need to be sufficiently fast to complete such studies in a reasonable span of time. Since nano-calorimeters can perform measurements orders of magnitude faster than traditional calorimeters, these sensors are ideal for high-throughput analysis.

While nanocalorimetry can measure thermodynamic properties and changes in state of a sample, it does not yield any structural information on the nature of the changes. High-intensity synchrotron radiation paired with area detectors, on the other hand, can quickly provide structural information on very small samples. Transmission synchrotron x-ray diffraction (S-XRD) and x-ray florescence spectroscopy have been used by Gregoire et al. to perform high-throughput crystallography analysis of thin film composition libraries [Gregoire 2009]. Recently, alternating current (AC) nanocalorimetry [Xiao 2012] was combined with S-XRD to perform simultaneous measurements of the structure and heat capacity of thin-film samples, using a similar transmission scattering geometry [Xiao 2013, Gregoire 2013]. This technique was used to analyze phase transformations in Bi, In, Sn, and FeNi thin-film samples at heating rates up to 300 K/s.

Direct current (DC) nanocalorimetry cannot typically operate at scanning rates below approximately 10^4 K/s because heat losses to the environment tend to overwhelm the signal. Measurements in the 10^3 K/s range require strong transformation signals and careful calculation or measurement of heat losses [Xiao 2014, Minakov 2005]. Synchrotron x-ray diffraction measurements, on the other hand, cannot be performed at scanning rates above 10^3 K/s for the samples like those in this study due to the lack of time-resolved signal at these high scan rates. Reactions of thick-multilayer foils at heating rates up to 10^6 K/s have been analyzed by S-XRD [Trenkle 2008]; however, such high rates are not possible for nanoscale films with complicating factors such as peaks from calorimeter-addendum phases. Thus, truly simultaneous DC nanocalorimetry and diffraction measurements are not possible with present technology. While the lower scans rates enabled by AC calorimetry are well suited for in situ S-XRD measurements [Xiao 2013], DC nanocalorimetry is required for certain experiments as it provides direct measurement of reaction enthalpy. In-situ measurements using DC calorimetry can be performed by acquiring S-XRD measurements during low- and high-temperature soaks, where each soak temperature is sufficiently far from reaction temperatures. This approach enables high-throughput acquisition of enthalpy-structure data on thin-film samples that would otherwise not be possible. The combination of DC nanocalorimetry with XRD is particularly useful for observing the cyclical-transformation behavior of materials and relating the enthalpy to structure evolution over time. Here the technique is used to study the behavior of the Ni-Ti-Hf martensite transformation as a function of composition and thermal cycling.

The Ni(Ti,Hf) compound of the Ni-Ti-Hf ternary alloy system is a shape memory alloy (SMA). This class of alloys is known for the solid-state transformation from a low-temperature, low-symmetry, martensite phase to a high-temperature, high-symmetry, austenite phase, which produces the well-known shape memory effect (SME). The base alloy, NiTi, has been the focus of considerable research efforts. It is the most important SMA from a practical standpoint, not only because of its good mechanical and shape memory properties, but also because of its good corrosion resistance and biocompatibility [Otsuka 2005]. The characteristics of the SME in NiTi depend sensitively on processing conditions and composition. Recent efforts have considered tailoring the SME of NiTi by alloying it with other elements such as Cu to reduce the thermal hysteresis [Zarnetta 2010], or Hf to increase the transformation temperature [Abujudom 1992]. Ni-Ti-Hf is seen as one of the most promising high-temperature SMA because it retains many of the positive aspects of the binary system, but with a significantly increased martensite-austenite transformation temperature. The results presented here provide guidelines for operating this materials system as a SMA in thin-film and nanocrystalline form.

What follows is a description of the in-situ nSC/S-XRD experimental technique and a demonstration of the measurement capabilities using Ni-Ti-Hf as a representative materials system. Results from nSC and S-XRD for Ni-Ti-Hf crystallization and martensite transformations are presented. The discussion includes an interpretation of the materials behavior and an assessment of the capabilities of the experimental technique.

Experimental description[1]

Parallel nano-scanning calorimeter

The nanocalorimetry measurements in this study were performed using a parallel nano-scanning calorimetry (PnSC) device. The PnSC is a micromachined device described in detail elsewhere [McCluskey 2006, McCluskey 2010a, McCluskey 2010b]. Briefly, it consists of a silicon substrate with a 5×5 array of independently controlled calorimeter sensors. Each sensor contains a tungsten four-point electrical probe that serves both as a heating element and a resistance thermometer. The tungsten probe is supported by and encapsulated in a freestanding silicon nitride membrane. Figure 1 shows a schematic of one such sensor. In a typical nanocalorimetry measurement, a thin-film sample is deposited through a shadow mask over the heating element between the two sensing leads. To activate the sensor, an electric current is supplied through the tungsten heating element, which results in Joule heating of the sample and addendum. The measured current and voltage are used to determine the power supplied to the sensor and the resistance of the heating element, which is calibrated to temperature using a procedure described in detail in references [McCluskey 2010a, McCluskey 2010b].

X-ray diffraction setup

The S-XRD measurements were performed at the A2 beamline at the Cornell High Energy Synchrotron Source (CHESS) using a transmission-geometry diffraction experiment (see Fig. 2) [Gregoire 2009]. A lightly sanded Si-111 double-crystal monochromator provided a 30 keV x-ray beam with a flux of 4.5×10^{10} photons per second in the 0.6 x 1 mm beam cross-section. A large-area pixel array detector (GE 41RT) optimized for efficient detection of high-energy x-rays was used to acquire diffraction data.

---

[1] The experimental set-up for this work is similar to previously published work by the same authors and the description here borrows significantly from a previous publication [Xiao 2013]. It is re-presented here for completeness.

A vacuum chamber was used to control the ambient atmosphere during the calorimetry measurements. It was sized with an internal diameter of 30 cm to accommodate a probe card with the PnSC device. To align the x-ray beam with each of the calorimeter samples, the entire chamber was mounted on a two-dimensional translation stage. Two polyimide windows (0.1 mm-thick), one upstream and one downstream, allowed the incident beam and diffracted beam to pass through the chamber. The chamber was evacuated with a turbo pump (Adixen MDP-5011) backed by a rotary vane pump (Edwards RV3). The chamber pressure was measured using thermocouple and ionization vacuum gauges (Kurt J Lesker 300 and 354). The chamber was evacuated to a base pressure of 1 mTorr during the measurements.

Measurement controls and data acquisition

The nanocalorimetry measurement system comprises several sub-systems; 1) digital/analog converters for control and acquisition of required signals, 2) a programmable current source for powering the PnSC sensors and for monitoring the current output, and 3) a signal conditioning unit to amplify the sensor's voltage response. The data acquisition electronics setup was similar to that described in References [McCluskey 2010b] and [Xiao 2012], with modifications to create a compact and portable system that would facilitate integration with the S-XRD experiment; a detailed description of the data acquisition system used in this experiment is provided in Reference [Xiao 2013]. Individual sensors on the PnSC device were selected by manually switching wire connections between the probe card and the data acquisition system. The integrated measurement system was controlled via a LabView® program on the user computer. For a given experiment, the schedule for the current applied to the calorimeter and for the XRD detector acquisition were prepared prior to the experiment; both the calorimetry and XRD acquisition systems were triggered with a user-activated TTL signal.

Procedures

After microfabrication of the PnSC device [McCluskey 2010b], each sensor on the device was calibrated by measuring the resistance of the heating element and its linear temperature coefficient as described in reference [McCluskey 2010a, McCluskey 2010b]. In particular, the PnSC device was placed in a vacuum furnace and the furnace temperature was stepped from room temperature to 443 K in approximately 15 K intervals. The vacuum furnace was filled with helium gas to ensure temperature uniformity within the chamber. At each temperature step, a DC current of 1 mA, which yielded negligible Joule heating, was passed through each sensor on the PnSC device and the voltage across the heating element was recorded. The resistance of the heating elements was found to increase linearly

with temperature over the temperature range related to the martensite transformation, in accordance with the previously detailed calibration of the resistance thermometers [McCluskey 2010a, McCluskey 2010b].

Samples were deposited on the PnSC by co-sputtering from three elemental targets using a magnetron sputter system (AJA, Int.). The deposition flux passed through a shadow mask to limit the sample to the sensing portion of the heating element. Samples were deposited in two consecutive depositions on separate rows of a single array of calorimeters with a goal of fabricating two identical sets of samples with five different compositions. The composition and thickness of the calorimeter samples were determined from calibration samples deposited immediately prior to the calorimeter samples, using energy dispersive x-ray spectroscopy (EDAX system installed on a Zeiss Ultra55 scanning electron microscope) and mechanical profilometry (Veeco, Dektak 6M), respectively. All three depositions were performed in identical conditions: an Ar pressure of 1.5 mTorr with gun powers of 64, 207 and 31 W to the Ni, Ti and Hf sputtering targets, respectively; the positioning of the sample holder and sputtering targets were also fixed for all depositions. The deposition time was selected to produce samples with a thickness of approximately 320 nm. The samples were capped with approximately 30 nm of sputtered silicon nitride immediately after deposition to prevent oxidation of the samples during crystallization. This sample preparation method has been shown to yield amorphous Ni-Ti-Hf thin films [Motemani 2011] , which was confirmed in this study through S-XRD characterization of the as-deposited samples.

The thickness, composition and mass of the samples are shown in Table 1. The sputter conditions were chosen such that the compositions of the samples varied substantially in Ti ($34.9 \leq f_{Ti} \leq 40.5$ at%) and Hf ($13.8 \leq f_{Hf} \leq 18.4$ at%) and minimally in Ni ($45.7 \leq f_{Ni} \leq 46.7$ at%). The sample mass was calculated using equation 1,

$$m_S = V_S \frac{2(f_{Ni}M_{Ni}+f_{Ti}M_{Ti}+f_{Hf}M_{Hf})}{100 N_A V_{UC}}, \qquad\qquad \text{Eq. 1}$$

where V_S is the sample volume as estimated from the sample thickness and area; the fractional term is the theoretical density of the material. Here N_A is Avogadro's number, M_{Xx} is the atomic mass of the respective element and the factor of 2 comes from the two atoms in the B2 austenite structure. The volume of the unit cell V_{UC} was calculated from the lattice parameter of the austenite phase obtained from the low-temperature XRD measurements and is a source of variation in the estimation of the sample mass.

Samples were crystallized at different heating rates to probe the kinetics of the transformation by applying a 74.6-86.6 mA current for slowly crystallized samples (odd numbered samples) and 107.9-109.5 mA for fast-crystallized samples (even numbered samples). This crystallization cycle was followed by multiple scans to probe the martensite transformation. These scans consisted of a temperature ramp and a seven second temperature hold (Fig. 3). The temperature ramp provided data for the nanocalorimetry measurement, while the high-temperature XRD data were acquired for seven seconds during the temperature hold. Low-temperature XRD was obtained during a seven second period after current flow to the sensor ceased and the sample equilibrated to ambient temperature.

Results and Discussion

Nanocalorimetry

Figure 4 shows the calorimetry curve for the crystallization of sample 8, i.e., the first calorimetry scan performed on the as-deposited sample. The curve is typical for all samples in this study and represents the raw calorimetric signal $P/\dot{T}$ (Eq. 2) [Efremov 2004, McCluskey 2010a] without any baseline correction,

$$\frac{P}{\dot{T}} = \frac{dH}{dT} + \frac{Q}{\dot{T}},$$
<div align="right">Eq. 2</div>

where P, T, and $\dot{T}$ are the power input, temperature, and heating rate of the sensor, respectively, while Q represents the heat loss to the environment. By performing appropriate reference measurements, it is possible to extract the change in enthalpy of the sample with temperature from this signal. Details of the analysis can be found in reference [McCluskey 2010a]. The crystallization curve (Fig. 4) shows that heat loss is relatively insignificant compared to heat capacity before crystallization, as indicated by the slowly increasing calorimetric signal up to approximately 700 K. At the onset of crystallization, the curve inflects and forms the crystallization peak. At the completion of the crystallization process, radiation losses dominate the signal. The crystallization results have been analyzed for crystallization peak temperature and heating rate (Table 2). A graph of the crystallization temperature as a function of heating rate does not provide any clear correlation, most likely because the range of heating rates employed in the experiments is too narrow.

After crystallization, the samples were cycled through the martensite-austenite (M-A) transformation (Fig. 5) by heating to at least 673 K at a rate of approximately 15 x 10^3 K/s. The M-A transformation

curves shown in figure 5(a) were obtained as the difference between the calorimetric signals from the crystallized and the as-deposited amorphous sample. Integration of transformation peak after subtraction of a linear baseline produces the transformation enthalpy [McCluskey 2010a]; dividing this result by the sample mass yields the specific enthalpy h, which is listed in Table 2 for all samples. Inspection of the results for the first cycle (Table 2) shows that only samples 4 through 9 have a reaction enthalpy that is significantly different from zero, i.e., only samples with a Hf content less than 16.9 at.% undergo a martensitic transformation. The transformation temperature of bulk Ni-Ti-Hf shape memory alloys is known to reduce abruptly for Ni concentrations above 50 at.% Ni [Abujudom 1992], as with the binary alloy Ni-Ti [Tang 1997]. It is proposed here that samples with Hf in excess of 16.9 at.% do not transform because their transformation temperature is below ambient, i.e., they remain in the austenite phase throughout the measurement. For this to occur, the Ni content in the austenitic phase should exceed 50 at.%. The increase in Ni content of the austenite phase as compared to the as-deposited sample is caused by the precipitation of the $(Ti,Hf)_2Ni$ phase [Motemani 2011]. Further evidence for the $(Ti,Hf)_2Ni$ phase and its effect on the M-A transformation behavior is presented later.

The specific enthalpy measured for the thin-film samples is on the low end of previously measured values for bulk materials, which range from 7.05 to 25.3 J/g [Meng 2010, Meng 2003]. It has been proposed that this reduction in enthalpy is due to the formation of the R-phase [Motemani 2011, Ren 2001]. The shape of the transformation signal in Figure 5(a) shows a double peak in the latter cycles, which is indicative of a 2-step transformation and may indicate the presence of the R-phase; however, R-phase diffraction peaks were not observed by XRD. More likely, the reduction in specific enthalpy is the result of two contributing factors: 1) only a fraction of the material is transforming and 2) the nano-crystalline grain size in these samples. The effect of a portion of the material transforming is clear; the specific enthalpy will vary directly with the fraction of material transforming. The residual austenite present at room temperature is shown in Table 3. Grain size, though not as obvious, can also affect transformation enthalpy. The average grain size as determined from the widths of the diffraction peaks of the austenite phase is 15 nm. Such a small grain size requires the formation of a martensite with an extremely fine twin structure, which increases the energy of the martensitic phase. Modeling by Waitz [Waitz 2007], which considers the energy penalty for forming martensite in nanocrystalline material can be used to show an expected one-third reduction in enthalpy when comparing the enthalpy of M-A transformations in 15 nm grain samples to 250 nm grain samples. Applying both corrections to the experimental values of the specific enthalpy provides an estimate of the specific transformation

enthalpy *h** for bulk samples (Table 2), the range of which very closely matches the previously reported bulk values.

Nominal transformation temperatures were taken as the temperatures at which half of the martensite had transformed to austenite, as determined by the area under the transformation peaks in the calorimetric signal (Fig. 5(b)). Note that the transformed-fraction curves in Figure 5(b) were produced by normalizing the peak areas with respect to the peak area in the first thermal cycle. The results of the analysis are listed in Table 2. The trend of increasing transformation temperature with Hf concentration shown in Table 2 is typical of this material [Abujudom 1992, Sanjabi 2005]. The transformation temperatures are, however, reduced compared to the bulk values because of the fine grain structure of the samples and the resulting nano-twinned martensite structure [Waitz 2007]. It has been shown that the interface energy associated with the martensite twins penalizes the formation of martensite and reduces the transformation temperature in nanocrystalline Ni-Ti [Waitz 2004], Ni-Ti-Zr [McCluskey 2011] and Ni-Ti-Hf [Motemani 2011]. It is notable that samples crystallized at slower heating rates have higher transformation temperatures than samples crystallized at faster heating rates. This is not a grain size effect since the grain size is independent of the heating rate, as determined by XRD. It is not the result of the precipitation of a second phase either, since a precipitate that changes the Hf content of the austenite would also produce a change in lattice parameter that is correlated with heating rate; this was not observed. This result demonstrates how sensitive the martensite transformation is to small changes in materials processing.

Cycling the samples through the martensite transformation and holding them at elevated temperature for the high-temperature XRD measurement reveals that the magnitude of the martensite transformation signal decreases with each cycle until it is near or below the detection limit. Hold temperatures are shown in Table 2. The decrease can be observed in the curves of Figure 5 and is quantified in Figure 6, which shows the reduction in calculated specific enthalpy as a function of cycle number, along with a linear least squares fit. This data processing was applied to each sample and the slope of each linear fit is provided in Table 2. The transformation temperatures generally decline with each cycle (Fig. 6(b) and Table 2) except for a few samples, which remain essentially unchanged. The drop in transformation temperature and enthalpy indicate that the material is precipitating $(Ti,Hf)_2Ni$. As Motemanni noted [Motemanni 2011], the precipitation of $(Ti,Hf)_2Ni$ increases the Ni concentration in the austenite-phase, which reduces the transformation temperature once Ni exceeds 50 at.% and thus prevents the reverse transformation as described previously. The effect is observed in samples held at

high and moderate temperatures showing that this mechanism can be active in these thin film samples at moderate temperatures, approximately 850 K, over short times, 7 seconds.

X-ray diffraction

The large atomic form factor of tungsten causes the diffraction pattern from the tungsten heating element to dominate the intensity of the diffracted spectra (Fig. 7). In order to reduce the contribution from the tungsten and to enhance the Ni-Ti-Hf diffraction pattern, the spectra of the as-deposited samples were subtracted from the spectra of the samples after crystallization. Prior to subtraction, all spectra were normalized with respect to the intensity of the {110} tungsten peaks. The resulting spectra clearly show the diffraction peaks associated with the Ni-Ti-Hf sample (Fig. 7). The lattice parameter of the austenite phase was calculated from the {110}, {200}, and {211} austenite diffraction peaks (Table 3). As expected, the lattice parameter increases with increasing Hf content, which has a larger atomic radius than both Ni and Ti.

Figure 8 shows the diffraction spectra obtained at ambient and elevated temperature for sample 8. Quantitative analysis was performed on the austenite phase only. While the peaks of the martensitic phase can be clearly discerned in the figure, the heights of the peaks are too small relative to background as a result of the twinned microstructure, preventing any meaningful analysis. The fraction of austenite in the samples was determined from the austenite peaks by comparing the intensities of the peaks under different conditions of temperature or heat treatment. In particular, the phase fraction was quantified by comparing the intensities of the {110} and {211} austenite peaks with the intensities of the same peaks during the first high-temperature hold. Since all transforming material was austenitic during the high-temperature XRD measurement, the austenite phase fraction can be estimated from the ratio of the observed intensity I_{110} and the theoretical intensity I_{110}^{th}, taking into account experimental correction factors as described in Appendix A. To incorporate the intensities from both the {110} and {211} austenite peaks, the phase fraction was calculated as

$$f_A = 1 - \left(\frac{I_{110}^{th}}{I_{110}^{H1}}\right)\left(\frac{I_{110}-I_{110}^{H1}}{I_{110}^{th}} + \frac{I_{211}-I_{211}^{H1}}{I_{211}^{th}}\right)/2, \hspace{2cm} \text{Eq.3}$$

where the superscript *H*1 refers to the first high-temperature hold. The {200} austenite peak (PDF 01-072-8487 (ICDD, 2006)) was omitted from the calculation because it overlaps with the {121} and {220} martensite peaks (PDF 04-008-5982 (ICDD, 2005)) [ICDD 2010]. The initial fraction of austenite at ambient temperature is tabulated for all samples in Table 3. The results demonstrate that samples with

10

more than 46.3% Ni consist mainly of austenite, while the austenite phase fraction drops significantly for lower Ni concentrations. These results confirm the nanocalorimetry findings. Indeed, for samples that transform, there is a strong correlation between the change in austenite phase fraction on transformation and the experimental transformation enthalpy.

The high-temperature diffraction data reveal the effect of thermal cycling and high-temperature holds on the phase composition of the samples. Figure 9 shows the austenite phase fraction for both a weakly (#3) and a strongly (#8) transforming sample. The weakly transforming sample starts with little difference between the high- and low-temperature phase compositions and both trend lower with increased high-temperature exposure. In contrast, the strongly transforming sample starts with a large gap in the high- and low-temperature phase compositions, but this gap narrows with thermal cycling. The high-temperature austenite fraction remains nearly constant for the strongly transforming sample compared to the weakly transforming sample. In fact, the reduction in high-temperature austenite phase fraction with cycling becomes more pronounced with increasing Hf content (Table 3). This result can be attributed to the precipitation of $(Ti,Hf)_2Ni$ from the matrix, which is more pronounced at higher Hf content. Ti_2Ni-based precipitates are, however, difficult to detect in the present XRD data, because the major peaks from Ti_2Ni are obscured by the martensite and much stronger austenite peaks (PDF 01-072-8487 (ICDD, 2006), PDF 04-008-5982 (ICDD, 2005), and PDF 04-007-1531 (ICDD, 2009)) [ICDD 2010]; higher scattering vector resolution and larger grain sizes would help to facilitate precipitate identification. $(Ti,Hf)_2Ni$ precipitates also tend to be very small [Zhang 2002, Meng 2010], which broadens the diffraction profile and weakens intensity. However, these precipitates have been observed by means of TEM in similarly prepared samples (Fig. 10) [Motemanni 2011].

$(Ti,Hf)_2Ni$ precipitates can also explain the convergence of the high- and low-temperature austenite phase fractions for strongly transforming samples. Figure 11 shows the difference between the high- and low-temperature phase fractions, averaged over the strongly and weakly transforming samples. Precipitation of just 6 at.% of $(Ti,Hf)_2Ni$ increases the nickel content of the matrix by 1 at.%, which is the entire range between weekly and strongly transforming samples: Precipitation of $(Ti,Hf)_2Ni$ lowers the transformation temperature and reduces martensite formation at room temperature. The change in lattice constants of the austenite phase with thermal cycling supports these findings. The lattice constant of the austenite phase decreases with thermal cycling (Table 3), in agreement with an enrichment of the phase in Ni and a depletion of Ti and Hf. The lattice constant of the matrix decreases

more quickly in samples with high Hf content, providing further evidence that the Hf enhances precipitation of the $(Ti,Hf)_2Ni$ phase.

A reduction in transformation temperature is generally undesirable for applications, but it is helpful from an instrumentation point of view to demonstrate the measurement technique. Specifically, the reduction in transforming phase fraction with cycling as determined by S-XRD (Fig. 11) can be compared to the specific enthalpy reduction obtained by nSC (Fig. 6(a)). The correlation of the signals for each sample is show in Table 3. The correlation coefficients for the weakly transforming samples, samples 1-3, are small and cannot be distinguished from zero with a 99% confidence level. The correlation is very strong for the remaining samples, 4 through 9. These results show that when there is a change in the signal the correlations between the S-XRD and nSC results are very strong. Thus it can be stated with a high degree of certainty that the reduction in enthalpy observed by nSC is caused by a reduction of the amount of transforming material.

Conclusion

Nano-scanning calorimetry and in-situ synchrotron x-ray diffraction are combined in a powerful technique to analyze enthalpy-related materials properties and structure information at low and high temperatures. The technique was used to crystallize amorphous Ni-Ti-Hf samples by local heating at rates of 8000 to 27,000 K/s, producing nano-crystalline thin-film samples. The change in austenite phase fraction was determined by low- and high-temperature XRD measurements, and integration with the nano-scanning calorimeter allowed correlation of the XRD results with the specific enthalpy as a function of composition. Finally, the high-temperature stability of the material was revealed with multiple cycles through the martensite transformation, followed by a high-temperature hold. The phase fraction by XRD and specific enthalpy by PnSC were strongly correlated, and were used to prove that the reverse transformation was gradually suppressed.

The cycling results for the thin-film samples of Ni-Ti-Hf with nanoscale grain structures show that the material has narrow operating conditions for a stable shape memory effect. For Ni concentrations above approximately 46.6 at.% Ni the transformation temperature becomes too low to rely on ambient cooling to cause the reverse transformation. For concentrations below 46.3 at.% Ni precipitation of $(Ti,Hf)_2Ni$ at elevated temperatures can increase the Ni concentration of the matrix and again suppress the reverse transformation. Operation of such a material requires low Ni concentrations and fast temperature cycles with limited exposure to high temperatures.

Integrating the PnSC and S-XRD enables high-throughput experimentation of thin-film samples, while providing thermodynamic and structural materials properties. High-throughput capabilities facilitate combinatorial studies, as envisioned in the development of the PnSC device. The combined high-throughput capabilities are also very well suited for studying the cyclical behavior of materials, by significantly reducing experiment times. Besides experimental convenience, fast cycling times are often required for studying nanoscale materials at elevated temperatures because of inherent instabilities of nanoscale structures. As the materials transition from the non-equilibrium to equilibrium state, fast cycling enables measurements during the transition.

Acknowledgement

Appendix A

X-ray diffraction experiments require calibration of the experimental setup to avoid systematic errors. Errors can arise from x-ray absorption, detector efficiency, geometric and polarization factors [Skinner 2012]. The calibration of the acquired intensities is described here in order to calculate the expected intensities and determine sample phase fractions. The presence of tungsten is normally undesirable because it creates intense peaks that can obscure desired sample peaks. Here, the presence of tungsten is advantageous because it can be used for calibration purposes. The expected intensity of an arbitrary peak is described by,

$$I_{hkl}^{Calc} = C(Q) \, M_{hkl} \, |S_{hkl}|^2, \tag{Eq. A1}$$

where $C(Q)$ is the experimental correction factor as a function of scattering vector magnitude Q, M_{hkl} is the plane multiplicity and S_{hkl} is the structure factor for a given plane. The experimental correction factor can be determined from,

$$C(Q) = \frac{I_{hkl}^{Meas}}{M_{hkl} |S_{hkl}|^2},$$

Eq. A2

using for I_{hkl}^{Meas} the intensities of the tungsten peaks obtained from the nSC device prior to crystallization of the Ni-Ti-Hf samples. Figure A1 shows the result of this calculation for the {110}, {200}, {211}, {220}, and {310} tungsten peaks along with a rational function fit, where the numerator and denominator of Eq. A2 have been normalized by the measured and calculated intensity of the W {110} peak, respectively. The fit represents the data with a residual no greater than 0.05. The austenite peaks analyzed to determine changes in phase fraction earlier in the paper have scattering vectors within the range of the {110} and {310} peaks. So the correction to the intensity of each peak is accurate to within 5% of the primary tungsten peak intensity. Equation A1 is used to calculate the expected austenite intensities and entered into Equation 3 in the main body of the paper.

References

Abujudom, D. N., Thoma, P. E., Kao, M. Y., & Angst, D. R. (1992). *Patent No. 5114504.* United States.

Anselmi-Tamburini, U., Ohyanagi, M., & Munir, Z. (2004). Modeling Studies of the Effect of Twins on the X-ray Diffraction Patterns of Boron Carbide. *Chemistry of Materials, 16*, 4347-4351.

Efremov, M. Y., Olson, E. A., Zhang, M., Lai, S. L., Schiettekatte, F., Zhang, Z. S., et al. (2004). Thin-film differential scanning nanocalorimetry: heat capacity analysis. *Thermochimica Acta, 412*, 13-23.

Efremov, M. Y., Schiettekatte, F., Olson, A. E., Kwan, A. T., Berry, R. S., & Allen, L. H. (2000). Discrete periodic melting point observations for nanostructure ensembles. *Physical review letters, 85*(17), 3560.

Gregoire, J. M., Dale, D., Kazimirov, A., DiSalvo, F. J., & van Dover, R. B. (2009). High energy x-ray diffraction/x-ray fluorescence spectroscopy for high-throughput analysis of composition spread thin films. *Review of Scientific Instruments, 80*(12), 123905.

Gregoire, J. M., McCluskey, P. J., Dale, D., Ding, S., Schroers, J., & Vlassak, J. J. (2012). Combining combinatorial nanocalorimetry and X-ray diffraction techniques to study the effects of composition and quench rate on Au–Cu–Si metallic glasses. *Scripta Materialia, 66*(3), 178-181.

Gregoire, J. M., Xiao, K., McCluskey, P. J., Cuddalorepatta, G., & Vlassak, J. J. (2013). In-situ X-ray diffraction combined with scanning AC nanocalorimetry applied to a Fe0.84Ni0.16 thin-film sample. *Applied physics letters, 102*(20), 201902.

ICDD. (2010). *PDF-4+ (Database).* (D. S. Kebekkodu, Ed.) Newton Square, PA, USA: International Centre for Diffraction Data.

Lai, S. L., Guo, J. Y., Petrova, V., Ramanath, G., & Allen, L. H. (1996). Size-dependent melting properties of small tin particles: nanocalorimetric measurements. *Physical Review Letters, 77*(1), 99.

McCluskey, P. J., & Vlassak, J. J. (2006). Parallel nano-differential scanning calorimetry: a new device for combinatorial analysis of complex nano-scale material systems. *Materials Research Society Proceedings*, 0924-Z08-14.

McCluskey, P. J., & Vlassak, J. J. (2010a). Combinatorial nanocalorimetry. *Journal of Materials Research, 25*(11), 2086-2100.

McCluskey, P. J., & Vlassak, J. J. (2010b). Nano-thermal transport array: An instrument for combinatorial measurements of heat transfer in nanoscale films. *Thin Solid Films, 518*(23), 7093-7106.

McCluskey, P. J., & Vlassak, J. J. (2011). Glass transition and crystallization of amorphous Ni–Ti–Zr thin films by combinatorial nano-calorimetry. *Scripta Materialia, 64*(3), 264-267.

McCluskey, P. J., Zhao, C., Kfir, O., & Vlassak, J. J. (2011). Precipitation and thermal fatigue in Ni–Ti–Zr shape memory alloy thin films by combinatorial nanocalorimetry. *Acta Materialia, 59*(13), 5116-5124.

Meng, X. L., Cai, W., Fu, Y. D., Zhang, J. X., & Zhao, L. C. (2010). Martensite structure in Ti–Ni–Hf–Cu quaternary alloy ribbons containing (Ti,Hf)2Ni precipitates. *Acta Materialia, 58*, 3751–3763.

Meng, X. L., Cai, W., Zheng, Y. F., Rao, Y. B., & Zhao, L. C. (2003). Two-way shape memory effect induced by martensite deformation and stabilization of martensite in Ti36Ni49Hf15 high temperature shape memory alloy. *Materials Letters, 57*, 4206-4211.

Minakov, A. A., Adamovsky, S. A., & Schick, C. (2005). Non-adiabatic thin-film (chip) nanocalorimetry. *Thermochimica Acta, 432*, 177-185.

Minakov, A. A., Mordvintsev, D. A., & Schick, C. (2004). Melting and reorganization of poly (ethylene terephthalate) on fast heating (1000 K/s). *Polymer, 45*(11), 3755-3763.

Motemani, Y., McCluskey, P. J., Zhao, C., Tan, M., & Vlassak, J. J. (2011). Analysis of Ti-Ni-Hf shape memory alloys by combinatorial nanocalorimetry. *Acta Materialia, 59*, 7602-7614.

Olson, E. A., Efremov, M. Y., Zhang, M., Zhang, Z., & Allen, L. H. (2003). The design and operation of a MEMS differential scanning nanocalorimeter for high-speed heat capacity measurements of ultrathin films. *Microelectromechanical Systems, 12*(3), 355-364.

Otsuka, K., & Ren, X. (2005). Physical metallurgy of Ti–Ni-based shape memory alloys. *Progress inMaterials Science, 50*, 511–678.

Queen, D. R., & Hellman, F. (2009). Thin film nanocalorimeter for heat capacity measurements of 30 nm films. *Review of Scientific Instruments, 80*, 063901.

Ren, X., Miura, N., Zhang, J., Otsuka, K., Tanaka, K., Kiowa, M., et al. (2011). A comparative study of elastic constants of Ti–Ni-based alloys prior to martensitic transformation. *Materials Science and Engineering A, 312*, 196–206.

Sanjabi, S., Cao, Y. Z., & Barber, Z. H. (2005). Multi-target sputter deposition of Ni50Ti50–xHfx shape memory thin films for high temperature microactuator application. *Sensors and Actuators A, 121*, 543–548.

Skinner, L. B., Benmore, C. J., & Parise, J. B. (2012). Area detector corrections for high quality synchrotron X-ray structure factor measurements. *Nuclear Instruments and Methods in Physics Research A, 662*, 61-70.

Tang, W. (1997). Thermodynamic Study of the Low-Temperature Phase B19' and the Martensitic Transformation in Near-Equiatomic Ti-Ni Shape Memory Alloys. *METALLURGICAL AND MATERIALS TRANSACTIONS A, 28A*, 537.

Trenkle, J. C., Koerner, L. J., Tate, M. W., Gruner, S. M., Weihs, T. P., & Hufnagel, T. C. (2008). Phase transformations during rapid heating of Al/Ni multilayer foils. *APPLIED PHYSICS LETTERS, 93*, 081903.

Waitz, T., Antretter, T., Fischer, F. D., Simha, N. K., & Karnthaler, H. P. (2007). Size effects on the martensitic phase transformation of NiTi nanograins. *Journal of the Mechanics and Physics of Solids, 55*(2), 419-444.

Waitz, T., Kazykhanov, V., & Karnthaler, H. P. (2004). Martensitic phase transformations in nanocrystalline NiTi studied by TEM. *Acta Materialia, 52*, 137–147.

Xiao, K., & Vlassak, J. J. (2014). Nucleation behavior of melted Bi films at cooling rates from 10^1 to 10^4 K/s studied by combining scanning AC and DC nano-calorimetry techniques. *Thermochimica Acta*, http://dx.doi.org/10.1016/j.tca.2014.05.006.

Xiao, K., Gregoire, J. M., McCluskey, P. J., & Vlassak, J. J. (2012). A scanning AC calorimetry technique for the analysis of nano-scale quantities of materials. *Review of Scientific Instruments, 83*, 114901.

Xiao, K., Gregoire, J. M., McCluskey, P. J., Dale, D., & Vlassak, J. J. (2013). Scanning AC nanocalorimetry combined with in-situ x-ray diffraction. *Journal of Applied Physics, 113*(24), 243501.

Zarnetta, R., Takahashi, R., Young, M. L., Savan, A., Furuya, Y., Thienhaus, S., et al. (2010). Identification of Quaternary Shape Memory Alloys with Near-Zero Thermal Hysteresis and Unprecedented Functional Stability. *Advanced Functional Materials, 20*, 1917-1923.

Zhang, J. X., Sato, M., & Ishida, A. (2002). Structure of martensite in sputter-deposited Ti-Ni thin films containing homogeneously distributed Ti2Ni precipitates. *PHILOSOPHICAL MAGAZINE A, 82*(7), 1433-1449.

Zhang, M., Efremov, M. Y., Schiettekatte, F., Olson, E. A., Kwan, A. T., Lai, S. L., et al. (2000). Size-dependent melting point depression of nanostructures: nanocalorimetric measurements. *Physical Review B, 62*(15), 10548.

Zink, B. L., Revaz, B., Sappey, F., & Hellman, F. (2002). Thin Film Microcalorimeter for Heat Capacity Measurements in High Magnetic Fields. *Review of Scientific Instruments, 73*, 1841.

Table 1: Physical Characteristics of Samples. Samples 2-9 are 4 pairs of identical samples.

Sample	Thickness	Mass	Composition		
(#)	(nm)	(μg)	Ni (at.%)	Ti (at.%)	Hf (at.%)
1	308	3.9	46.7	34.9	18.4
2	307	3.8	46.6	36.5	16.9
3	307	3.9	46.6	36.5	16.9
4	329	4.7	46.3	37.9	15.8
5	329	4.7	46.3	37.9	15.8
6	332	4.1	45.8	39.5	14.7
7	332	4.1	45.8	39.5	14.7
8	320	3.9	45.7	40.5	13.8
9	320	4.0	45.7	40.5	13.8

Table 2: nano-Scanning Calorimetry Results.

Sample	Crystallization		1st Martensite cycle			High-T-XRD	Martensite trend	
(#)	dT/dt (K/ms)	Temp. (K)	Enthalpy ± 0.6 (J/g)	h* (J/g)	$T_{\text{M-A}}$ ± 1 (K)	Temp. (K)*	dh/dc (J/g/cycle)	dT/dc (K/cycle)
1	Partial cryst.		-0.5	-5 ± 6	NA	746 ± 35	0.12 ± 0.04	NA
2	27.2	919	0.8	6 ± 5	NA	827 ± 39	-0.04 ± 0.03	NA
3	11.5	865	0.9	12 ± 8	NA	1170 ± 31	0.02 ± 0.02	NA
4	26.4	856	2.0	21 ± 6	393	879 ± 39	-0.09 ± 0.01	-0.9 ± 0.4
5	9.3	864	12.4	27 ± 1	421	1231 ± 29	-0.59 ± 0.09	0.5 ± 0.4
6	23.6	846	10.1	23 ± 1	383	842 ± 40	-0.62 ± 0.03	-1.8 ± 0.1
7	Corrupted data		3.6	7 ± 1	396	1097 ± 33	-0.36 ± 0.04	-2.1 ± 0.4
8	24.6	851	3.4	9 ± 1	362	825 ± 39	-0.24 ± 0.02	-0.66 ± 0.09
9	7.96	873	2.5	8 ± 2	372	983 ± 35	-0.12 ± 0.03	0.4 ± 0.2

* Average temperature of the sensor ± temperature non-uniformity estimated from thermal modeling of the sensor [Xiao 2012].

Table 3: X-ray Diffraction Results.

Sample	Austenite fraction - room temp.	Initial lattice constant	Trend in austenite at elevated temp.	Cyclical nSC-XRD correlation	Trend in lattice constant
		pm*	%/cycle	PCC	0.1pm/cycle
1	0.85 ± 0.05	307.5 ± 0.1	-4.79 ± 0.30	-0.53	-1.5 ± 0.1
2	0.81 ± 0.05	307.0 ± 0.2	-2.14 ± 0.22	0.30	-0.46 ± 0.04
3	0.89 ± 0.05	306.3 ± 0.1	-3.05 ± 0.07	-0.23	-0.95 ± 0.06
4	0.86 ± 0.05	306.7 ± 0.3	-2.18 ± 0.11	0.88	-0.58 ± 0.02
5	0.33 ± 0.05	306.8 ± 0.1	-1.87 ± 0.06	0.95	-0.69 ± 0.04
6	0.37 ± 0.05	306.6 ± 0.3	-1.30 ± 0.04	0.99	-0.35 ± 0.03
7	0.24 ± 0.05	305.3 ± 1.3	0.20 ± 0.15	0.97	-0.20 ± 0.05
8	0.43 ± 0.05	305.9 ± 0.6	-0.67 ± 0.06	0.96	-0.19 ± 0.03
9	0.54 ± 0.05	305.2 ± 1.3	-0.09 ± 0.12	0.83	-0.55 ± 0.08

* The lattice constant uncertainties do not include systematic error from calibration of the Q axis and are intended for relative changes in lattice constant.

Figure 1: Layout of the nanocalorimeter sensor: (a) cross-section schematic, and (b) plane-view schematic. Heater line-width is 0.8 mm and voltage probe line-width is 0.1 mm (after McCluskey et al. [McCluskey 2010a]).
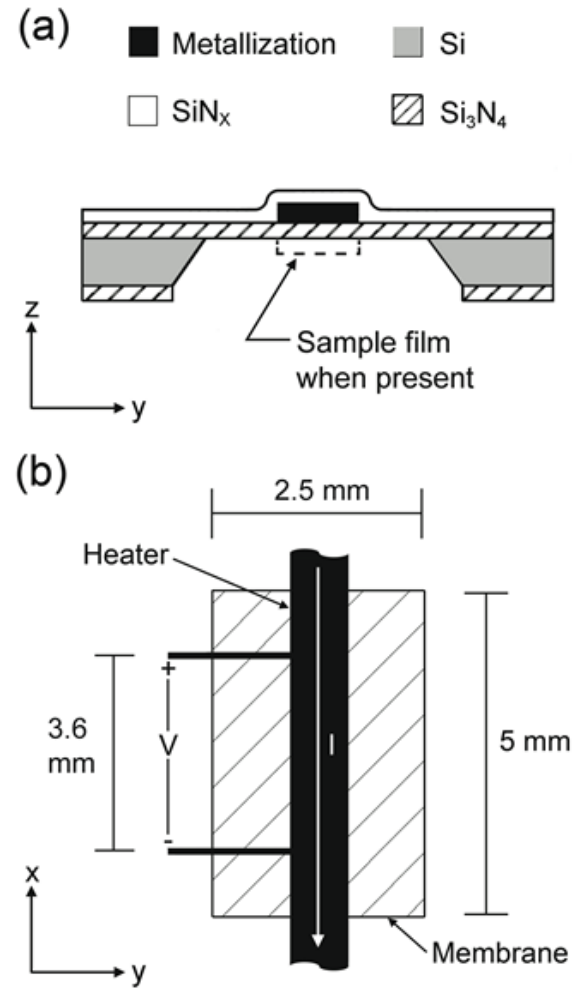
Figure 2: Experimental set-up for nano-scanning calorimetry and in-situ x-ray diffraction, the parallel nano-scanning calorimeter is located inside the chamber for calorimetry and XRD measurements (After Xiao et al. [Xiao 2013]).
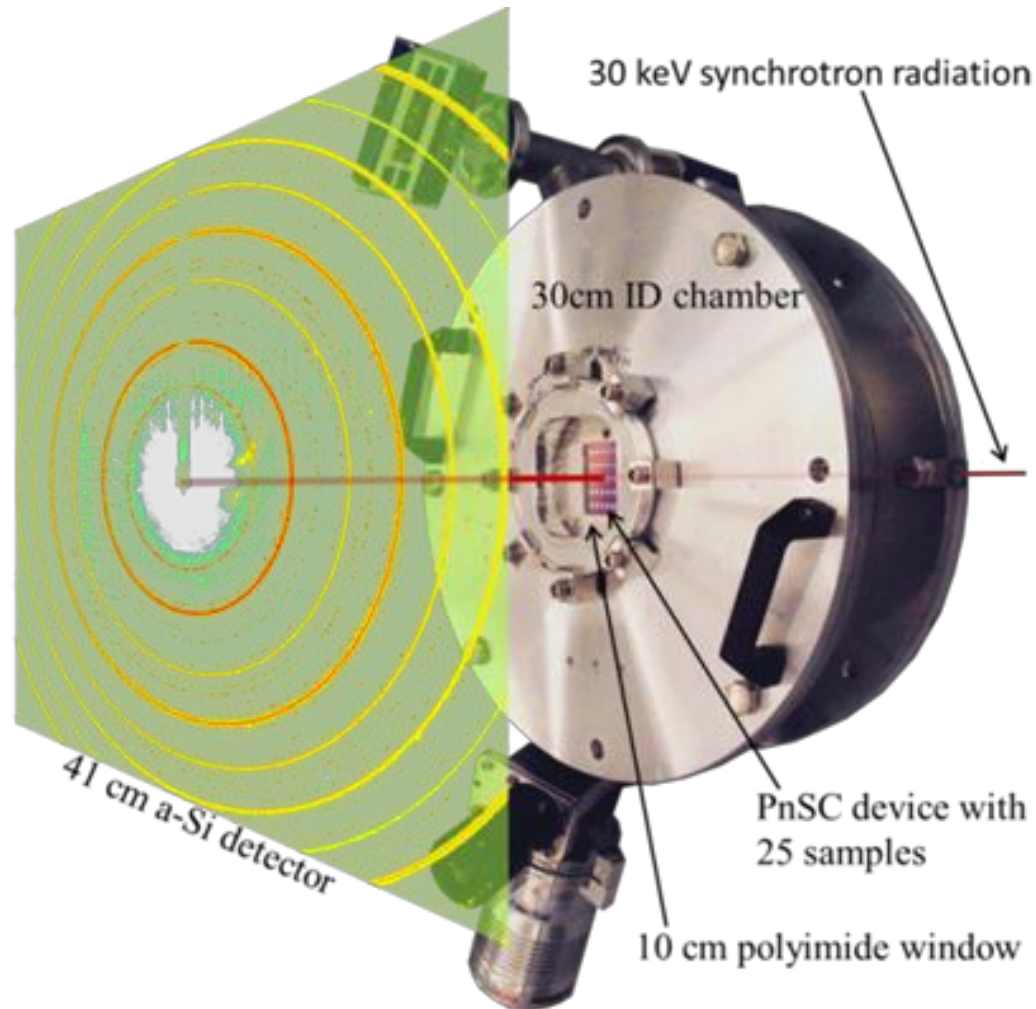
Figure 3: Sample 1 - current and voltage curves for a typical martensite cycle with nanocalorimetry and XRD acquisition time-periods indicated. During low-temperature XRD t < 7.0 s no current is applied and then a 94 mA is applied for 0.03 s during the nanocalorimetry portion of the cycle and finally high-temperature XRD is acquired when t > 7.3 s for seven seconds during which a 74 mA current is applied.
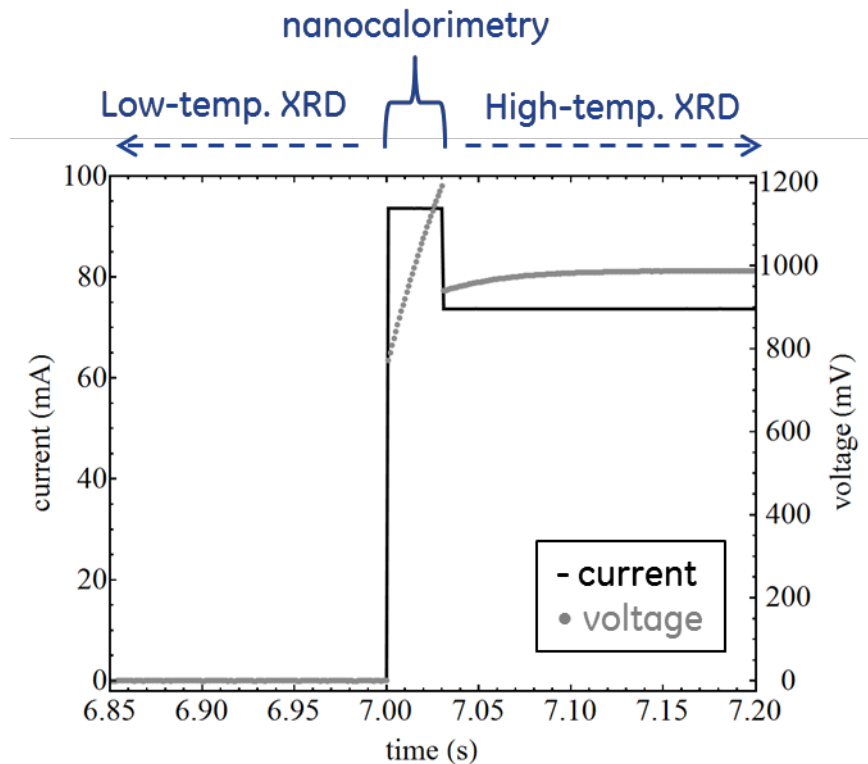
Figure 4: Sample 8 - raw crystallization curve.
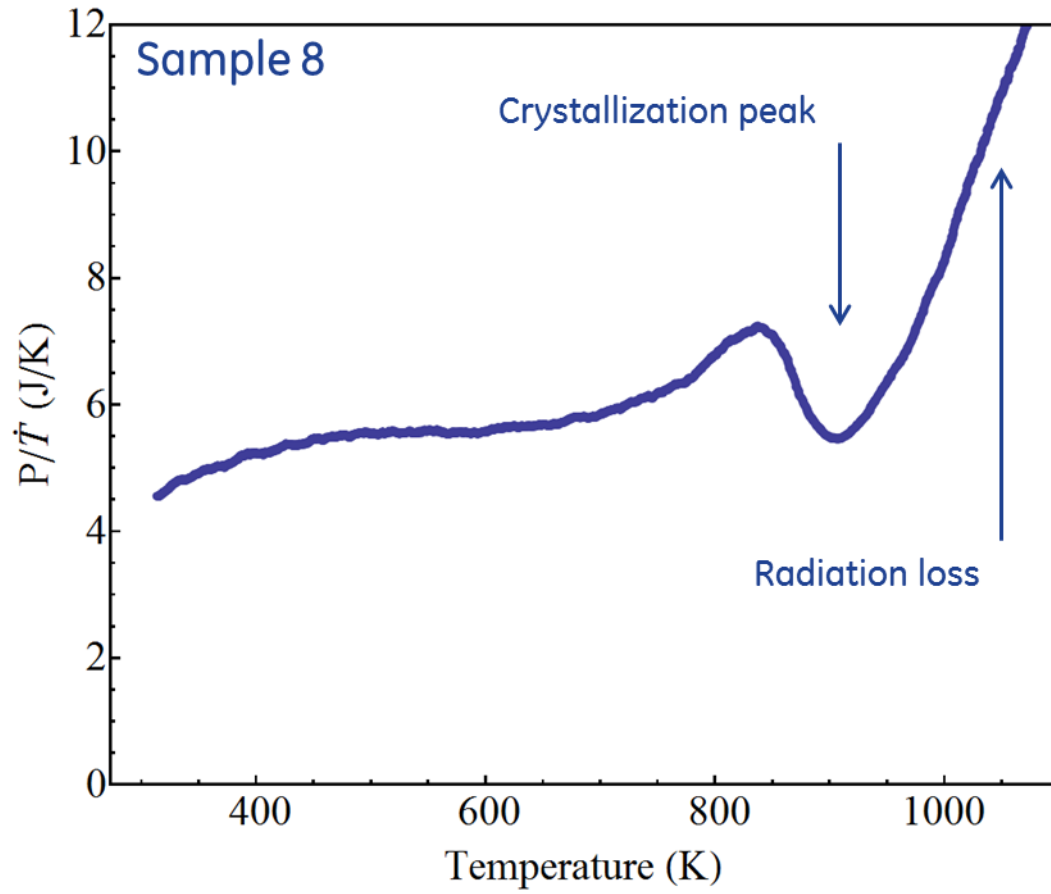
Figure 5: Martensite-austenite transformation peak (a) and transformed fraction (b) with cycling (sample 6).
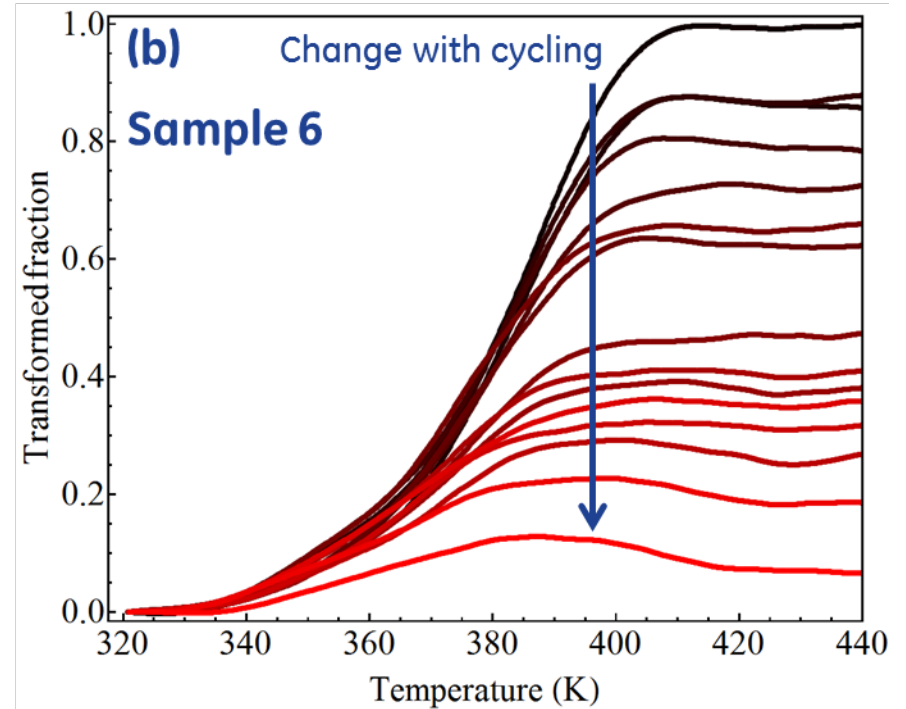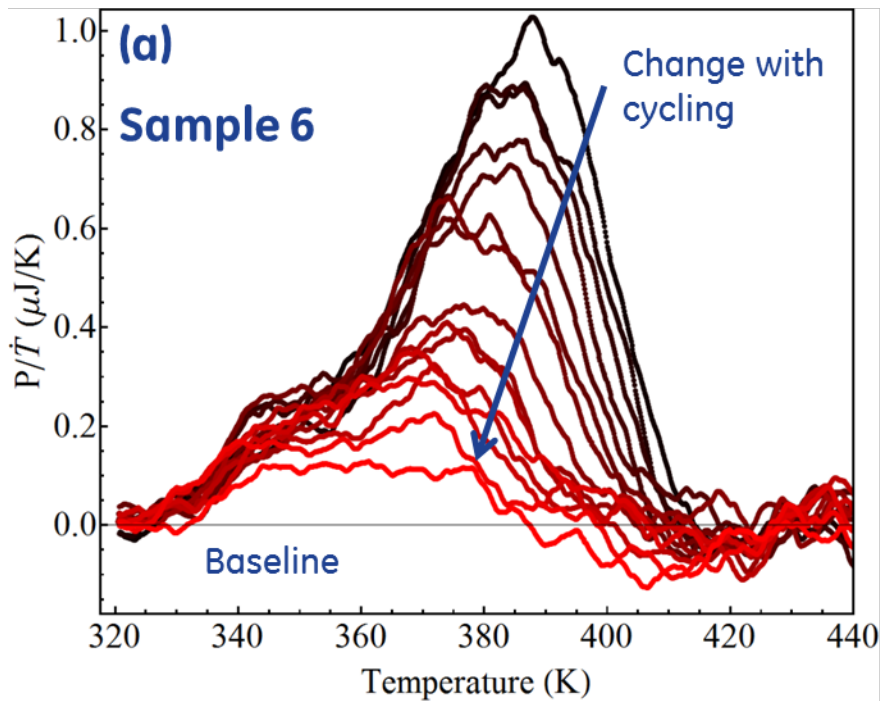
Figure 6: Martensite-austenite transformation enthalpy (a) and temperature (b) with cycling for sample 6.
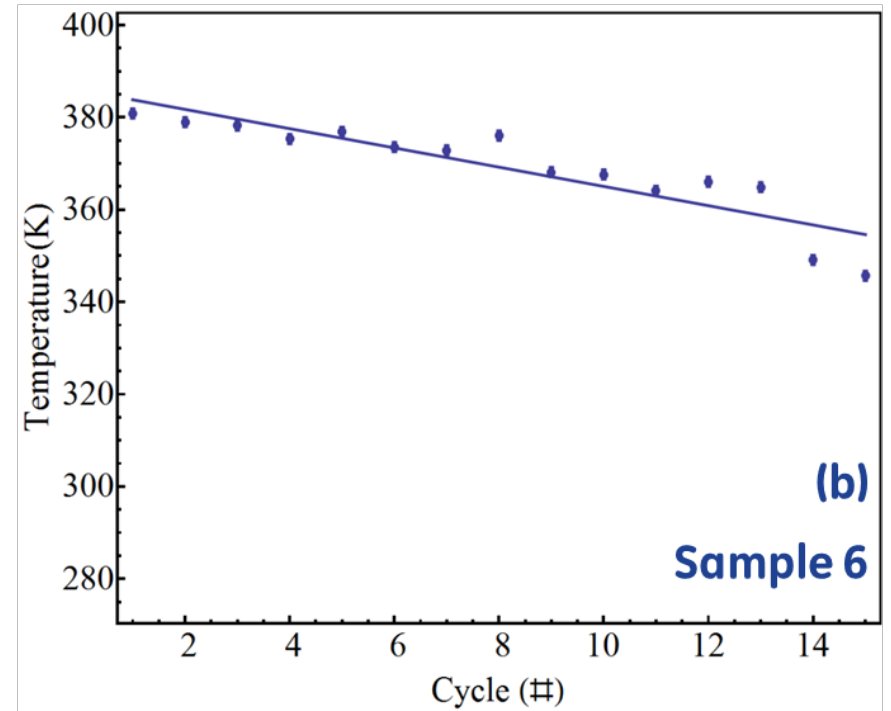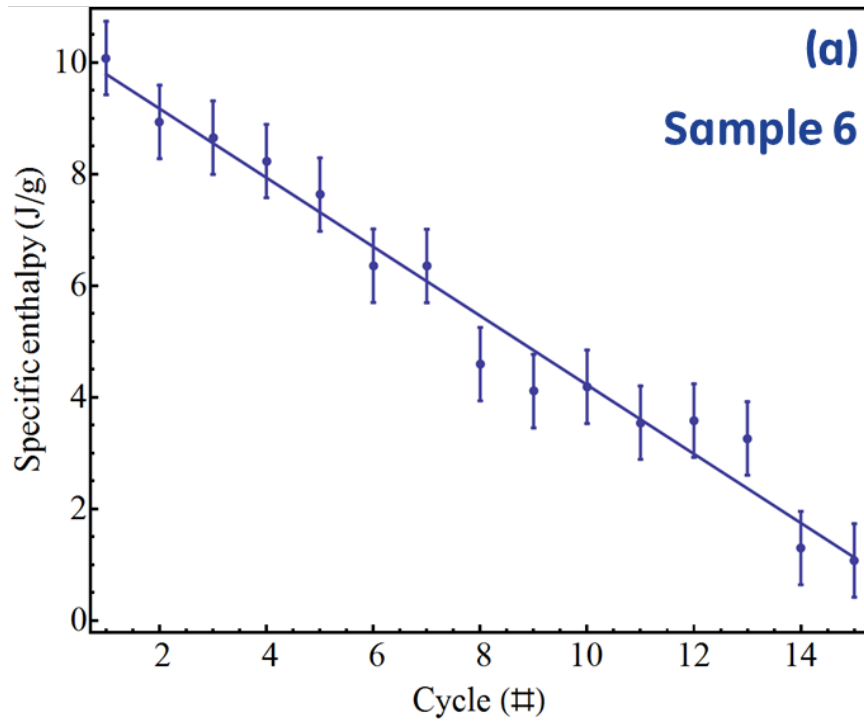
Figure 7: Ambient temperature XRD spectra for sample 1 before crystallization (offset for clarity), after crystallization, and difference spectra (note magnified scale). Tungsten, polyimide, and austenite peaks are labeled as W, P, and A, respectively.
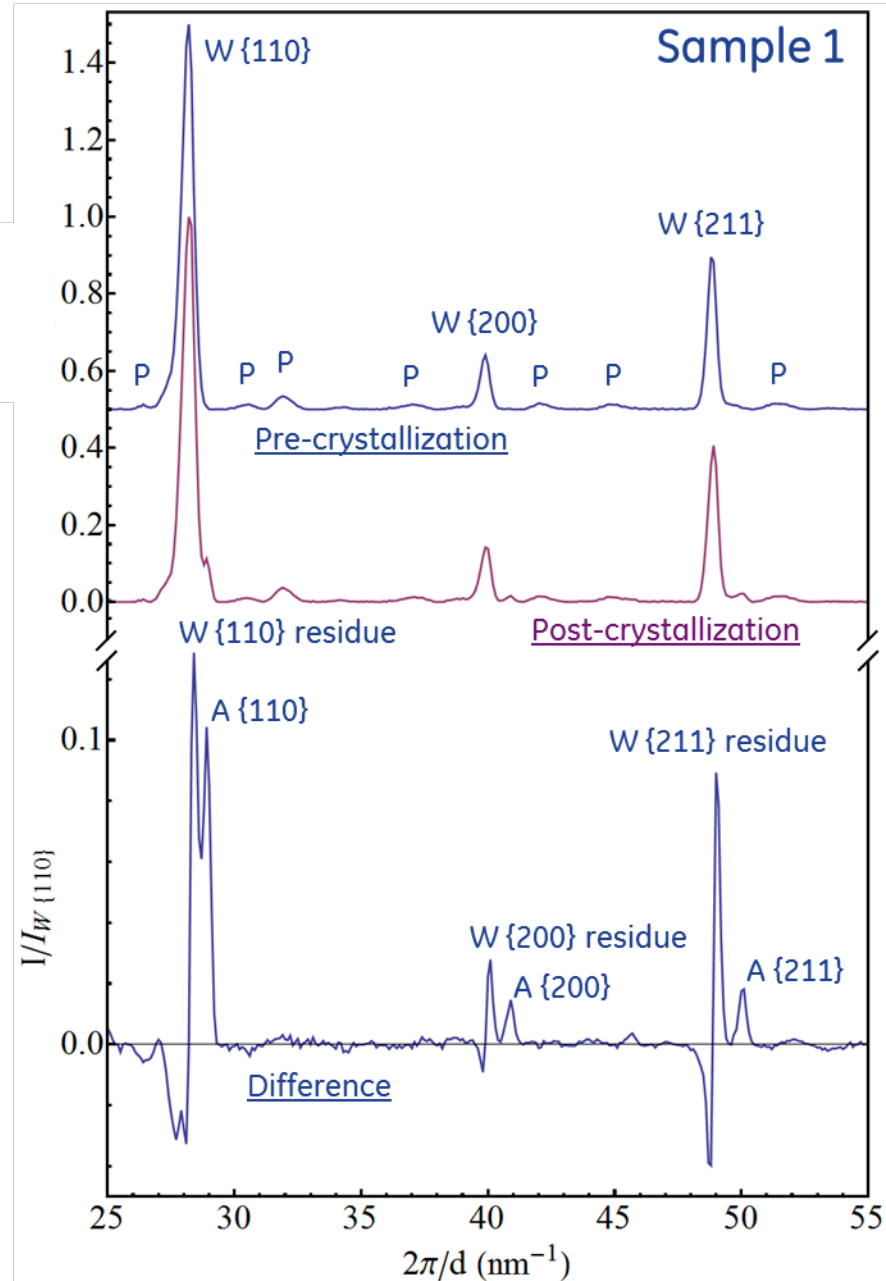
Figure 8: Difference XRD spectra for sample 8 with cycling at ambient temperature (black to green (a)) and elevated temperature (black to red (b)). Tungsten, austenite , and martensite peaks are labeled as W, A, and M, respectively.
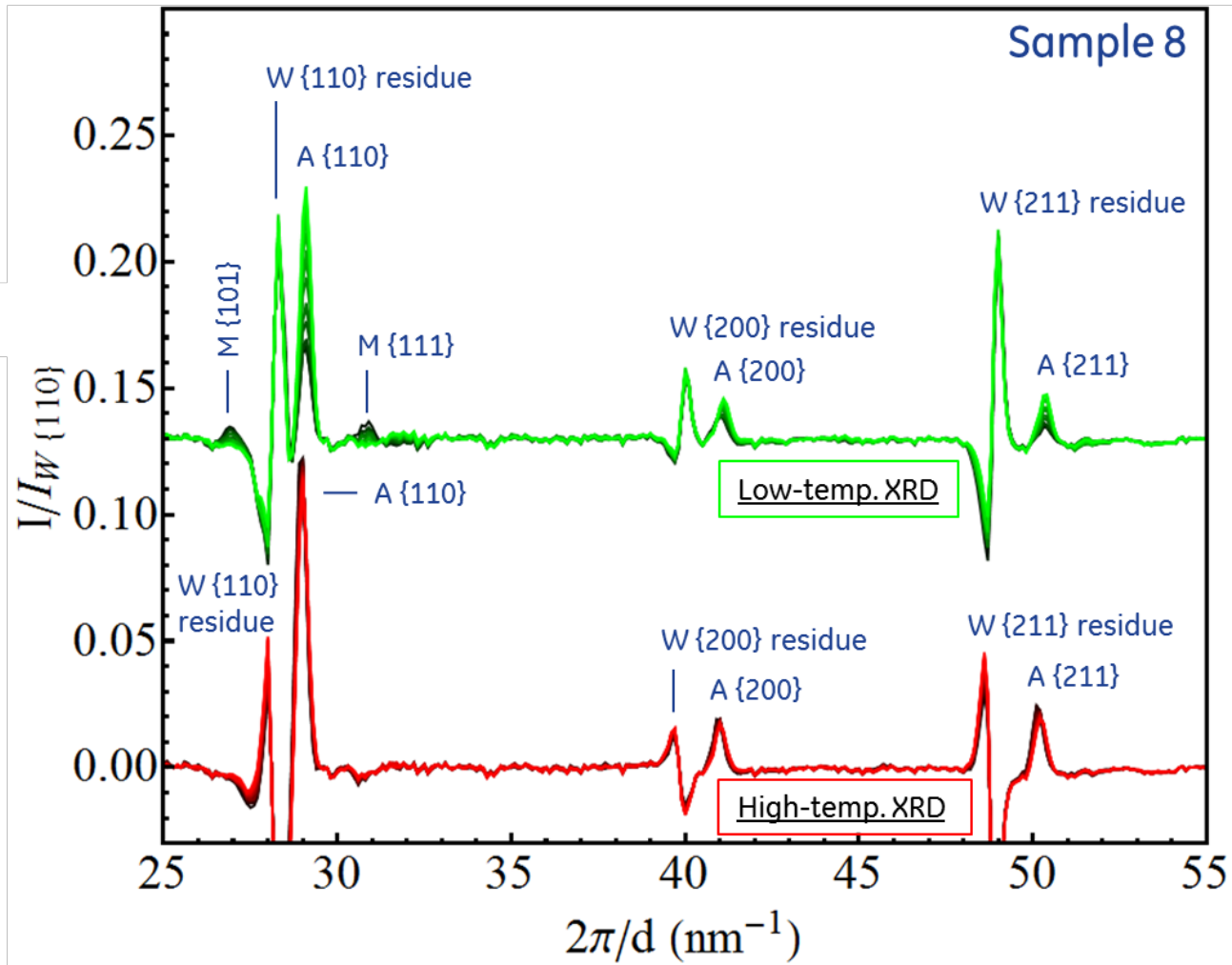
Figure 9: Trends in austenite phase fraction at high (f_A^{HT}) and low (f_A^{LT}) temperatures relative to initial state at high-temperature for a weakly transforming sample (#3) and strongly transforming sample (#8).
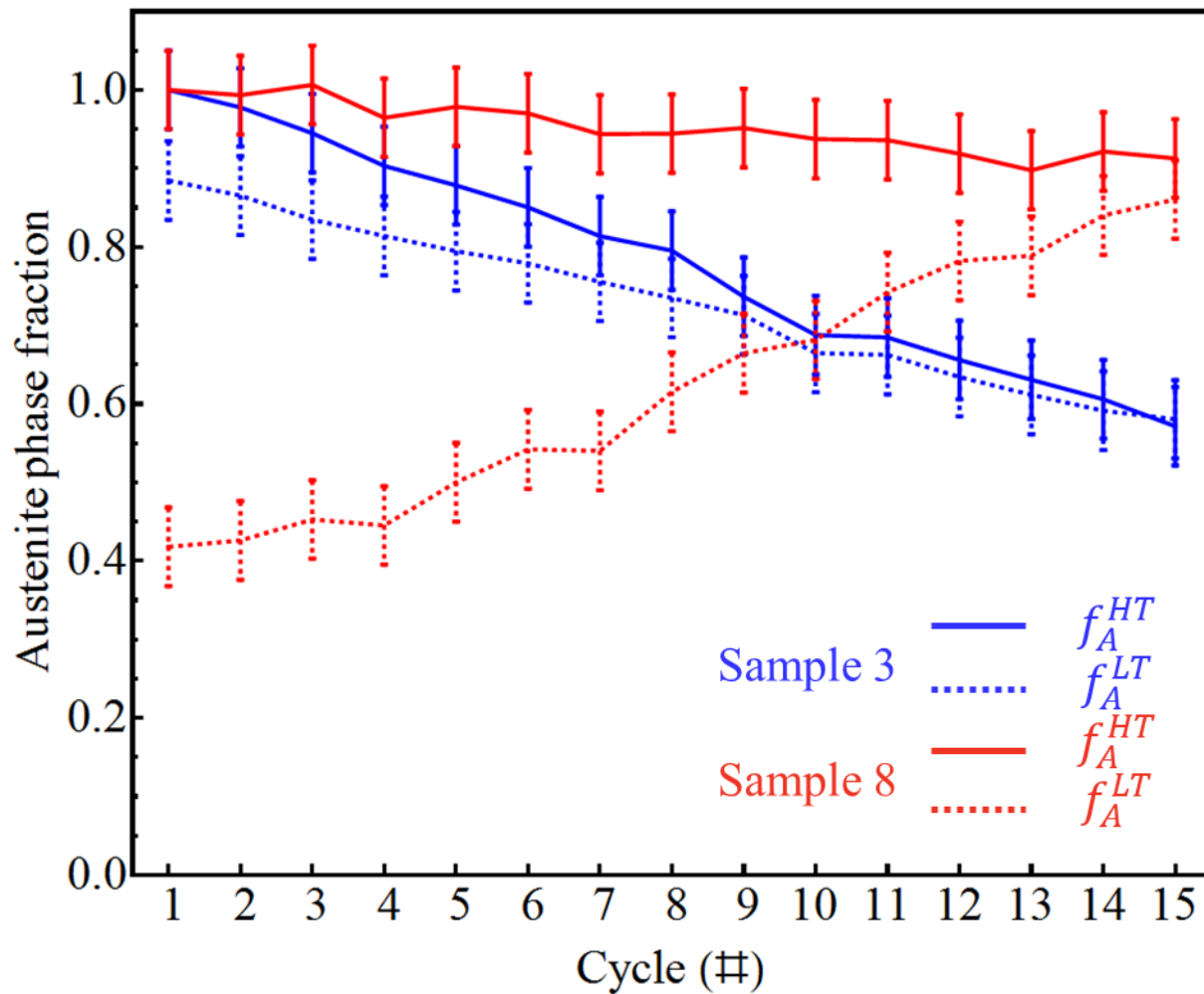
Figure 10: TEM micrograph (a) and corresponding electron diffraction pattern (b) for a thin film Ni-Ti-Hf sample crystallized by PnSC (after Motemanni et al. [Motemanni 2011], note that cell label is from prior publication).
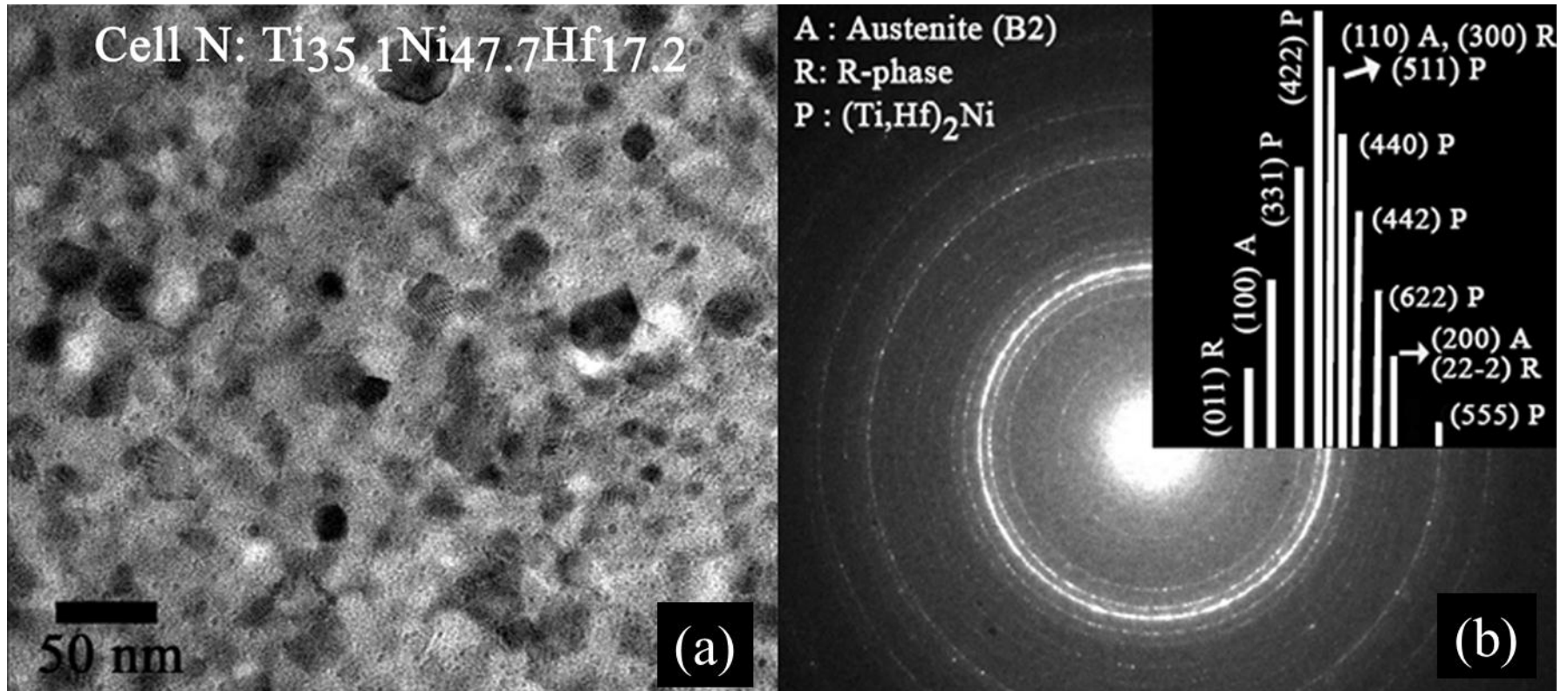
Figure 10: Average change in austenite phase fraction, high-temperature minus low temperature ($f_A^{HT} - f_A^{LT}$), for transforming (samples 5-9) and non-transforming cells (samples 1-4).
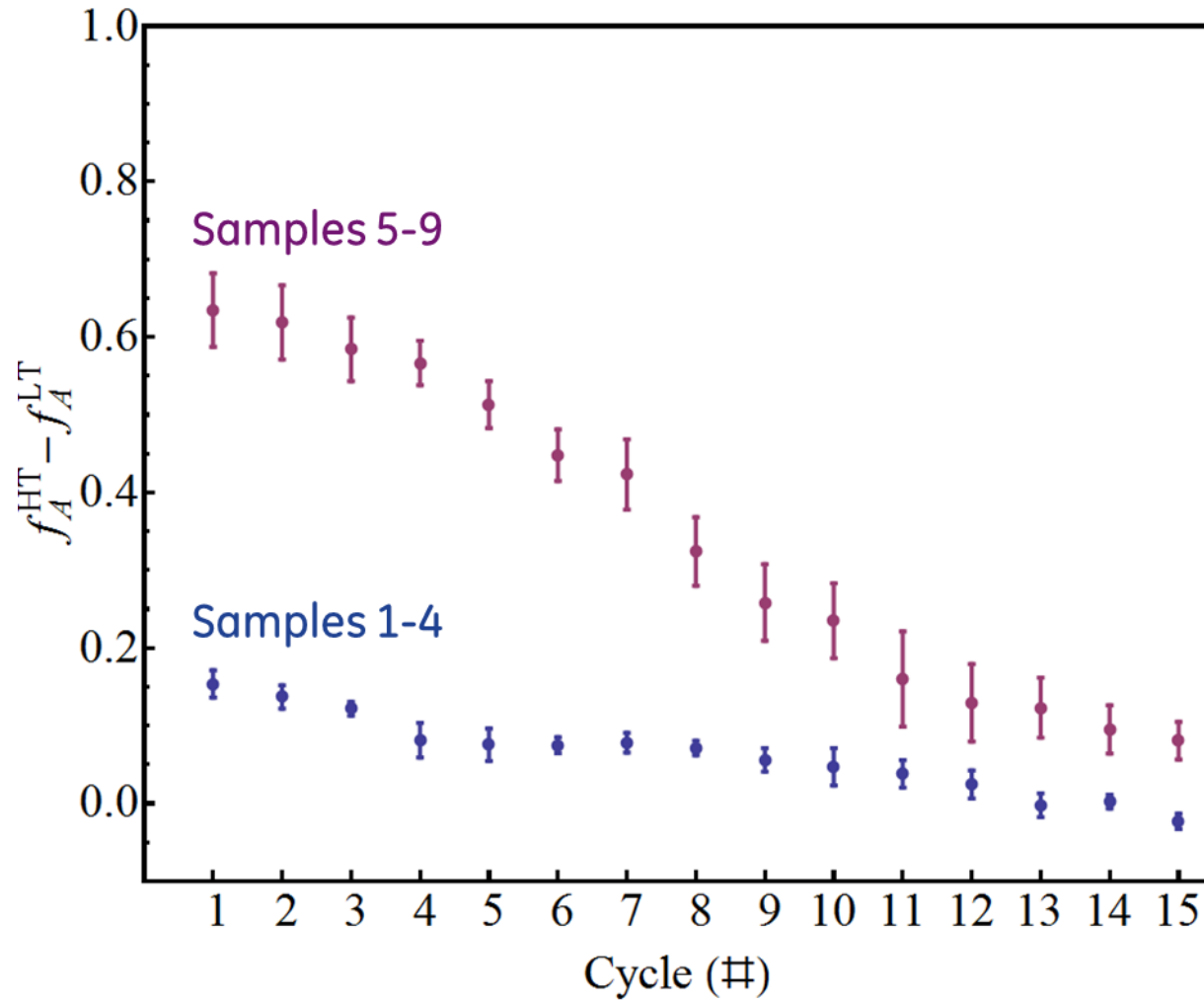
Figure A1: Experimental correction factor for instrument intensity as a function of scattering vector magnitude; fit to the average W intensities of all cells (I_{hkl}^{Ave}) divided by the uncorrected theoretical values ($M_{hkl} |S_{hkl}|^2$) using the rational function $(1 + a x)/(b + c x)$. The positions of the austenite peaks used for calculating phase fraction are shown for reference.